THE JOURNAL OF PHYSICAL CHEMISTRY C

Article

Cite This: J. Phys. Chem. C 2019, 123, 30604−30612

pubs.acs.org/JPCC

Phonon Dynamics in Anisotropic Dilute $CuAl_{1-x}Fe_xO_2$ Delafossite Alloys by a Weighted Dynamical Matrix Approach

M. Aziziha,[†] S. Akbarshahi,[†] S. Ghosh,[‡] P. Pramanik,[‡] J. P. Lewis,[†] A. H. Romero,[†] S. Thota,[‡] M. S. Seehra,[†] and M. B. Johnson*[,†]

[†]Department of Physics & Astronomy, West Virginia University, Morgantown, West Virginia 26506, United States

[‡]Department of Physics, Indian Institute of Technology, Guwahati, Assam 781039, India

Supporting Information

ABSTRACT: Here we report a new versatile approach for the calculation of phonon modes which is applicable to anisotropic, dilute alloys with allowance for a large variety of alloying elements. This approach has significant advantages over previously reported methods, especially for the lattice dynamics of such complex alloys. We use this approach to model the effects of Fe-doping on the vibrational modes in dilute alloys of $CuAl_{1-x}Fe_xO_2$ (x = 0, 0.01, 0.05, and 0.10) delafossite powders. These samples were structurally characterized with X-ray diffraction (XRD) combined with Rietveld refinement to measure their lattice parameters and Raman and FTIR spectroscopies to measure optical phonon frequencies. To compare experimental results from XRD with calculations for lattice parameters, we use a disordered supercell for x in the range 0−0.1. Both results agree well with Vegard's law. For the phonon calculations, an approach using a disordered supercell is not feasible because it is too computationally expensive. Instead, we developed our weighted dynamical matrix (WDM) approach that uses a straightforward ordered supercell for force-constant calculations of the $CuAlO_2$ and $CuFeO_2$ parent end points, and combines them using a WDM approach leading to an effective medium for vibrational mode calculation in random alloys. Computationally, when Fe is substituted for Al (increasing x), an increase in the bond length is observed leading to a red-shift in the peak positions in all of the phonon modes vs x, in agreement with the experimentally observed trend.

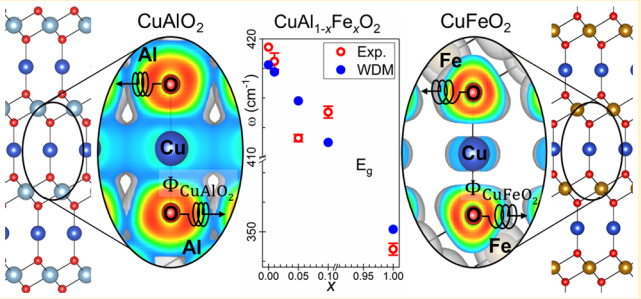

1. INTRODUCTION

Delafossites (AMO_2 with A: Cu or Ag; M: Al, Ga, La, Fe, or Cr) are one of a number of families of less-studied complex oxides with many attractive properties.[1−9] In particular, $CuAlO_2$ is a p-type wide-band-gap compound, an attractive candidate for transparent conductive oxide applications.[1−6] For $CuAlO_2$ thin films, the reported indirect and direct allowed optical band gaps are 1.8 and 3.5 eV, respectively.[2,10] It has been suggested that doping $CuAlO_2$ with transition metal ions, such as Fe, Mn, Ni, etc., may modify the indirect band gap, which is otherwise forbidden due to symmetry considerations.[11] $CuAlO_2$ has an indirect fundamental band gap, which is due to phonon-assisted optical transitions. On the other hand, alloying leads to chemical disorder in the lattice and causes phonon scattering.[12] Therefore, understanding the vibrational properties of $CuAl_{1-x}Fe_xO_2$ alloys is key to understanding the variation of optical (photon−phonon interaction) and electronic (electron−phonon interaction) properties with Fe concentration. To that end, we investigated the structural, electronic, magnetic, and optical properties of Fe-doped $CuAlO_2$. In recent papers,[13,14] we have reported on the synthesis of $CuAl_{1-x}Fe_xO_2$ (x = 0, 0.01, 0.05, and 0.10) samples followed by their structural characterization using X-ray diffraction (XRD), X-ray photoelectron spectroscopy (XPS), and scanning electron microscopy with energy dispersive spectroscopy, and magnetic investigations using vibrating sample magnetometry.

In this paper, vibrational modes observed for dilute $CuAl_{1-x}Fe_xO_2$ alloys using Raman and Fourier transform infrared (FTIR) spectroscopies are directly compared with the results obtained by first-principle calculations, to better understand these modes and the effect of Fe dopants.[15−17] The calculation of vibrational frequencies (phonon spectra) in dilute anisotropic alloys is not a simple undertaking, and the successful methodologies are not well developed. For this reason, our original approach started with the accurate calculations of the lattice structure of the dilute alloys using a disordered supercell. However, to continue and use these results to determine the phonon spectra, especially for dilute anisotropic alloys, is too computationally demanding. Instead, effective medium approaches must be used. One such approach, the virtual crystal approximation (VCA) is well-known for alloy calculations, but it does not work well for nonisoelectronic alloying elements like Al and Fe.[18] Another

Received: October 6, 2019
Revised: November 18, 2019
Published: November 19, 2019

DOI: 10.1021/acs.jpcc.9b09402
J. Phys. Chem. C 2019, 123, 30604−30612

such approach is the coherent potential approximation (CPA), which works best for isotropic lattices[19] but not for highly anisotropic lattices like the delafossites, and, in the case of dilute alloys, it is computationally demanding.[20,21] Based on these issues, we do not use VCA or CPA to model the vibrational characteristics of these dilute anisotropic alloys. In principle, the calculation of the vibrational frequencies can be done based on the supercell results; however, these calculations are only tractable in the case of the parent structures, $CuAlO_2$ and $CuFeO_2$, at the end points. Again, for the alloys, especially the dilute alloys, the very large supercells make the calculations too computationally demanding. For these reasons, we developed a new effective-medium approach using a weighted dynamical matrix (WDM), based on modifying the masses and interatomic force constants after calculation of Hellmann−Feynman forces[22] for parent compounds $CuAlO_2$ and $CuFeO_2$ (details given in section 2.2.2). There have been several attempts to consider mass and force-constant disorder in random alloys[23−30] The approach presented here is straightforward and computationally efficient and works well for dilute anisotropic $CuAl_{1-x}Fe_xO_2$ alloys.

2. METHODS

2.1. Experimental Section. Polycrystalline powder samples of $CuAl_{1-x}Fe_xO_2$ (x = 0, 0.01, 0.05, and 0.10) were prepared by the solid-state reaction method using Cu_2O, Al_2O_3, and α-Fe_2O_3 as precursors in appropriate stoichiometric ratios with heat treatment in static air at 1100 °C.[31] The details of these procedures along with structural, chemical, and magnetic characterization are given in recent papers.[13,14] Room temperature Raman spectra (200−2500 cm^{-1}) were acquired using a Horiba Jobin-Yvon LabRAM HR800 system (Ar ion laser, λ = 488 nm, spectral resolution of 1.5 cm^{-1} with a 2000 lines/mm grating). To obtain good signal-to-noise ratio, the laser was focused on the powder samples with a 10× objective and autoexposed for 15 accumulations using 100% the laser power (50 mW). Room temperature FTIR spectra (400−4000 cm^{-1}) were acquired using a PerkinElmer Spectrum-Two system (spectral resolution 0.5 cm^{-1}). FTIR samples were made using the KBr pellet method, with pellets oven-dried at 90 °C to remove adsorbed/absorbed moisture prior to acquiring the FTIR spectra.

2.2. Computational. Our computational strategy is the following: we use the supercell approach to determine the crystal structure/lattice parameters of the $CuAl_{1-x}Fe_xO_2$ alloys for x = 0, 0.01, 0.05, 0.1, and 1.0 (see section 2.2.1) using the Vienna Ab initio Simulation Package (VASP 5.4.4). The vibrational properties are computed through an effective medium approach, where we use an ordered supercell for $CuAlO_2$ and $CuFeO_2$ to determine their interatomic force constants and use these with our weighted dynamical matrix approach to calculate the phonon spectra.

2.2.1. Lattice Parameter Calculations. The lattice parameters for $CuAl_{1-x}Fe_xO_2$ are calculated in its ground-state energy configuration using VASP.[32−34] Relaxation of the conventional unit cell is done with an 8 × 8 × 2 Γ-centered k-point mesh and kinetic energy cutoff of 600 eV. The relaxed conventional unit cell with rhombohedral structure ($R\bar{3}m$) of $CuAlO_2$ is used to construct a 3 × 3 × 1 supercell containing 108 atoms. We use projector-augmented wave pseudopotentials[35] with the valence-electron configurations $3p^6 3d^{10} 4s^1$, $3p^6 3d^7 4s^1$, $3s^2 3p^1$, and $2s^2 2p^4$ for Cu, Fe, Al, and O, respectively. There are many possible configurations for Fe substituting for Al, but most of them can be ruled out by symmetry considerations, which is done by site-occupation disorder (SOD 0.47) code.[36] The relaxation of this disordered supercell is done with a 4 × 4 × 2 Γ-centered k-point mesh and a 600 eV kinetic energy cutoff. The relaxation method used leaves the supercell volume, positions, and cell shape free to change. Due to the strong correlation effects of Fe d electrons, we used a simplified (rotationally invariant) PBEsol+U approach[37,38] with an on-site Coulomb parameter U_{eff} = 4.6 eV and included spin polarization for Fe. To find the optimized U, the band gap, lattice parameters, magnetic moment, and Raman modes of $CuFeO_2$ are compared with the reported experimental values.

2.2.2. Weighted Dynamical Matrix (WDM) Approach. To find the phonon modes, one needs to construct the dynamical matrix. To do so, $\mathbf{r}_{li}$, the deviation of the ith atom in the lth unit cell of the supercell from equilibrium position, is introduced. Also, the second-order force constants for the li−$l'i'$ atom pair, denoted as $\Phi_{\alpha\beta}(0i, l'i')$ (with α and β indices for coordinates), are calculated. Then, the dynamical matrix $\mathbf{D}(\mathbf{q})$ at the wavevector $\mathbf{q}$ is constructed as follows:

$$\mathbf{D}_{ii'}^{\alpha\beta}(\mathbf{q}) = \frac{1}{\sqrt{m_i m_{i'}}} \sum_{l'} \Phi_{\alpha\beta}(0i, l'i') \exp[i\mathbf{q}\cdot(\mathbf{r}_{l'i'} - \mathbf{r}_{0i})] \quad (1)$$

where m_i is the mass of the ith atom. Phonon frequencies $\omega(\mathbf{q}, \kappa)$ and mode eigenvectors $\chi(\mathbf{q}, \kappa)$ at $\mathbf{q}$, where κ is the band index, are obtained by solving the eigenvalue equation:

$$\mathbf{D}(\mathbf{q})\,\chi(\mathbf{q}, \kappa) = [\omega(\mathbf{q}, \kappa)]^2\,\chi(\mathbf{q}, \kappa) \quad (2)$$

This proposed approach is tested and compared to our experimental results for $CuAl_{1-x}Fe_xO_2$. To calculate the phonon modes for these alloy samples, first the Hellmann−Feynman forces of the parent structures ($CuAlO_2$ and $CuFeO_2$), for atomic displacement of 0.01 Å from their equilibrium positions, are calculated by DFT calculations. Then from forces $\vec{F}_{CuAlO_2}$ and $\vec{F}_{CuFeO_2}$, the force constants Φ_{CuAlO_2} and Φ_{CuFeO_2} are calculated. The weighted dynamical matrix is constructed as follows:

$$\bar{\mathbf{D}}_{ii'}^{\alpha\beta}(\mathbf{q}) = \frac{1}{\sqrt{m_i m_{i'}}} \sum_{l'} \bar{\Phi}_{\alpha\beta}(0i, l'i') \exp[i\mathbf{q}\cdot(\mathbf{r}_{l'i'} - \mathbf{r}_{0i})] \quad (3)$$

where $\bar{\Phi} = x\Phi_{CuFeO_2} + (1 - x)\Phi_{CuAlO_2}$ refers to the weighted force constant, where x refers to Fe concentration. Also, we consider a pseudoatom instead of an M-site atom ($CuMO_2$) with mass as $m_M = xm_{Fe} + (1 - x)m_{Al}$ in eq 3. The advantage of our approach is that it can be easily used to estimate the interatomic force constants. Importantly, *any* percentage of dilute alloys can be considered, unlike the approach using a disordered supercell, which requires a very large supercell to represent a dilute alloy. However, there are some limitations to this approximation. First, by replacing Al with Fe, the Brillouin zone volume decreases, but this is not considered in the weighted dynamical matrix. Thus, we assume that this decrease does not influence the systems with dilute dopants. Also, in this method, we consider a pseudoatom M instead of Al and Fe. Then, in the projected density of states, the partial density of states from the individual Al and Fe atoms cannot be identified; only the constructed pseudoatom M is available. This lack of identification implies that we do not consider the

DOI: 10.1021/acs.jpcc.9b09402
J. Phys. Chem. C 2019, 123, 30604−30612

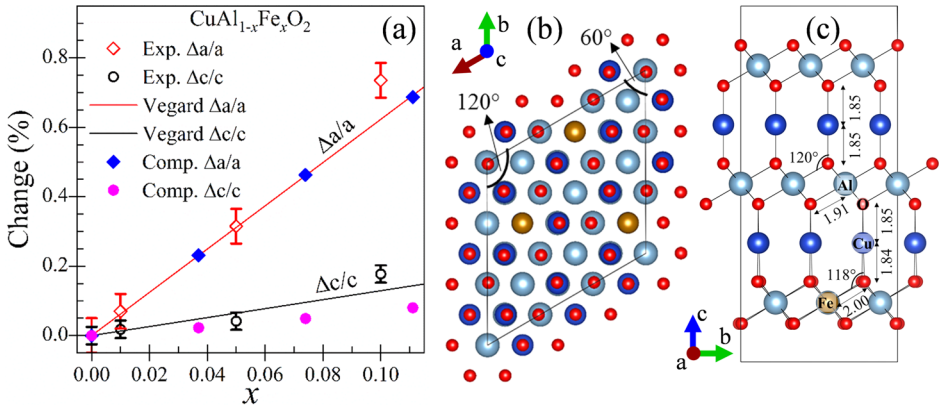

Figure 1. (a) Experimental data with error bars for percentage change of a and c vs x for $CuAl_{1-x}Fe_xO_2$ (with x = 0, 0.01, 0.05, and 0.10). Computed lattice parameters for disordered supercell of $CuAl_{1-x}Fe_xO_2$ are shown by solid squares and circles. Lines show the fit of the experimental data to Vegard's law. (b,c) Minimum energy disordered supercell configuration for x = 0.11 along the a- and c-axes.

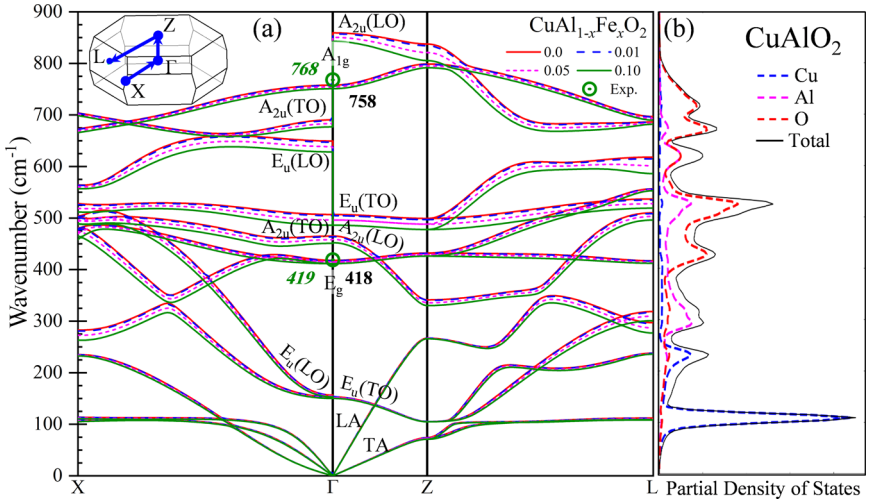

Figure 2. (a) Phonon dispersion for $CuAl_{1-x}Fe_xO_2$(x = 0, 0.01, 0.05, and 0.10) in the path marked in the Brillouin zone (inset), calculated by the WDM method. The experimental values for two Raman modes for x = 0.0 are marked as hollow circles. (b) Phonon density of states in the Brillouin zone.

effect of Fe-alloying on the electronic dielectric permittivity or the Born-effective charges, which account for the long-range interaction of the macroscopic E-field induced by the polarization of collective ionic motions near the Γ-point. We are further investigating the versatility of this proposed approach by comparing our method to the experimental and computational data for other structures, and we will report our results in a follow-up paper. Similar approaches, using only mass renormalization[39−41] or mass and force-constant renormalization, have been developed previously.[26−29] By considering only the weighted average mass, the decrease in the phonon modes does not agree well with experimental data. This highlights the fact that the simple weighted average mass alone does not work well due to the presence of strain and the improvements for weighted averaging the interatomic force constants along with the masses are necessary. Detailed features of our calculations include interatomic force constants calculated for parent compounds $CuAlO_2$ and $CuFeO_2$ primitive unit cells (relaxation done with 8 × 8 × 8 Γ-centered k-point mesh and kinetic energy cut off increased to 600 eV for both structures); supercells of 3 × 3 × 3 with 0.01 Å displacement are created,[42] and then forces (with 4 × 4 × 4 Γ-centered k-point mesh) and Born-effective charges and electronic dielectric permittivity (with 16 × 16 × 16 Γ-centered k-point mesh) are calculated with VASP.

3. RESULTS AND DISCUSSION

3.1. Structural Properties. To aid in our interpretation of Raman and FTIR results on the $CuAl_{1-x}Fe_xO_2$ samples, we briefly summarize the structural properties reported in our recent publications.[13,14] The XRD spectra of all four samples are refined by the Rietveld method,[43,44] and the changes in the lattice parameters a and c are calculated from the values resulting from the refinement. The details of this Rietveld analysis are shown in Figure S1. By substituting Fe for Al as an Fe^{3+} ion, the rhombohedral symmetry is unchanged, but the lattice expands with the relative expansion along the a-axis being ∼6 times larger than that along the c-axis. Figure 1a shows the variation of the lattice parameters a and c with change in Fe-doping. The solid lines show the Vegard's law fit. The DFT calculations are done on the disordered supercells of $CuAl_{1-x}Fe_xO_2$ for x = 0.0, 0.04, 0.08, and 0.11, and the lattice parameters are calculated for the ground-state configuration. The disordered supercell for x = 0.11 along the a- and c-axes is shown in Figure 1b and c. Our computational results show good agreement with the experimental data and fit to Vegard's

DOI: 10.1021/acs.jpcc.9b09402
J. Phys. Chem. C 2019, 123, 30604−30612

law.[45,46] Small deviations from Vegard's law may be due to the fact that our calculations are done at 0 K, whereas the experiments are done at room temperature. Bond lengths are marked in Figure 1c. These results imply that the substitution of Fe^{3+} for the smaller Al^{3+} (ionic radii 0.065 and 0.054 nm, respectively) introduces localized strain to the lattice and the M−O (M = Al, Fe) bond lengths increases with higher Fe doping. The bonds around substituted Fe atoms become distorted, and the M−O bond length increases (Al−O and Fe−O bonds are 0.191 and 0.200 nm, respectively) whereas the Cu−O bond length decreases from 0.185 to 0.184 nm near the dopant. These changes in the bond lengths affect the lattice parameters and vibrational modes.

3.2. Phonon Dynamics. *3.2.1. Phonon Dispersion.* Here, we present the calculated phonon modes for $CuAl_{1-x}Fe_xO_2$ (x = 0, 0.01, 0.05, and 0.1). Figure 2a shows the phonon dispersion for four doping concentrations along the X−Z−Γ−L paths (Brillouin zone is shown, inset). For $CuAlO_2$, with its four-atom primitive cell, there are 12 vibrational modes from group theory. At the Γ-point (Brillouin zone center), the modes have the symmetry: $\Gamma = E_g + A_{1g} + 3A_{2u} + 3E_u$. There are three acoustic modes with $\Gamma_{acoustic} = A_{2u} + E_u$ symmetry and zero frequency; two Raman-active modes E_g (doubly degenerate) and A_{1g}; and six IR-active modes of E_u and A_{2u}, which are optical phonons. The experimental values for these two Raman modes are marked as hollow circles to compare with experiment. In our calculations, we consider Born-effective charges by a nonanalytical term added to the dynamical matrix that breaks the degeneracy in the doubly degenerate modes. In general, longitudinal optical (LO) modes have higher frequency than transverse optical (TO) modes do. By alloying Fe in $CuAlO_2$, there is a clear decrease in the peak frequencies (red-shift) associated with the larger ionic radius and mass of Fe atoms that leads to a decrease in the interatomic force constants and an increase in the weighted average mass of the alloys compared to $CuAlO_2$.

In Figure 2b, the partial density of phonon states for $CuAlO_2$ is plotted as a function of the wavenumber over the whole Brillouin zone. Cu states are more noticeable at low frequencies (<250 cm^{-1}). E_g and A_{1g} Raman-active modes at Γ are only influenced by the vibration of oxygen, as discussed in the next section, whereas the IR-active modes are the result of vibrations of all the atoms (see Figure 7). The vibrational configurations along with the experimental data are presented below.

3.2.2. Raman Spectra. Raman spectra for the $CuAl_{1-x}Fe_xO_2$ samples are shown in Figure 3. For x = 0, there are two prominent peaks identified as E_g at 419 cm^{-1} and A_{1g} at 768 cm^{-1}, in addition to some weaker peaks. These peak identifications follow the Raman studies (measurements and modeling for single-crystal $CuAlO_2$) by Pellicer-Porres et al.[47] Experimentally, they see a peak at 767 cm^{-1} corresponding to the calculated A_{1g} mode at 770 cm^{-1} involving the vibration of O atoms along the c-axis (parallel to the O−Cu−O bonds) and a peak at 418 cm^{-1} corresponding to the calculated E_g at 433 cm^{-1} involving the vibration of O atoms perpendicular to the c-axis (in the hexagonal plane containing the a-axis). Other Raman studies in $CuAlO_2$[48−51] also reported the observations of these E_g and A_{1g} modes. In our powders, as doping level x increases, the prominent E_g and A_{1g} peaks get broader and weaker, and increasingly red-shifted. Also, a broad background peak centered around 600 cm^{-1} and a second broad peak centered around 1,300 cm^{-1} appear in the Fe-doped samples.

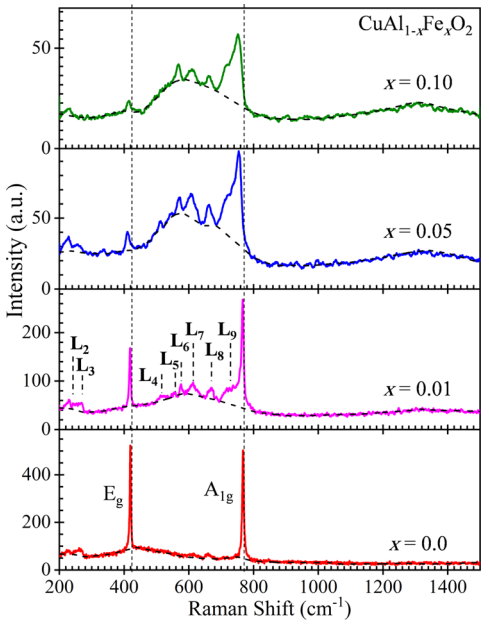

Figure 3. Raman spectra of $CuAl_{1-x}Fe_xO_2$, x = 0, 0.01, 0.05, and 0.10. A_{1g} and E_g modes are Raman-active. Data is smoothed by averaging adjacent points. Dashed lines show the background. For x = 0.01, peaks L_2−L_9 (weak modes) are labeled.

In addition to the E_g and A_{1g} modes, the spectra in Figure 3 also include several weaker peaks. These weaker peaks are similar to those reported for single crystals of $CuAlO_2$,[47] where the peaks are associated with intrinsic defects (Cu vacancies and interstitial oxygen) that result in p-type conductivity in $CuAlO_2$. Following the nomenclature used in,[47] the observed peaks are labeled L_2 through L_9 on Figure 3. The positions of these peaks vs. x are plotted in Figure 4. The solid symbol on

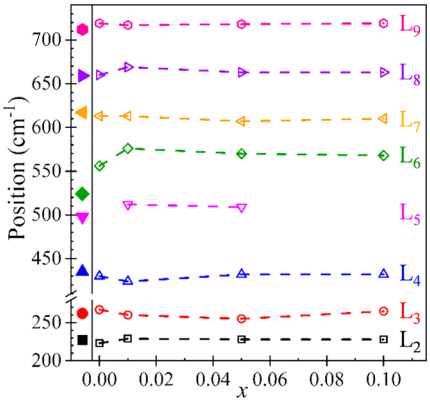

Figure 4. Wavenumber positions of observed weak Raman modes for $CuAl_{1-x}Fe_xO_2$ samples vs x from sample defects (open symbols). Experimental weak modes for x = 0, from ref 6 (solid symbols to left of x = 0), are shown for comparison.

the left frame, show the experimental positions of the peaks for $CuAlO_2$ reported by Pellicer-Porres et al.[47] The L_9 peak along with the broad modes at approximately 600 and 1300 cm^{-1} are observed only for the Fe-doped samples and not for $CuAlO_2$. It is likely that the broad mode at 1300 cm^{-1} is a second-order peak of the 600 cm^{-1} broad mode because similar second-order Raman peaks have been reported in other systems, such as graphitic samples.[52]

DOI: 10.1021/acs.jpcc.9b09402
J. Phys. Chem. C 2019, 123, 30604−30612

To determine the position, the full width at half-maximum (fwhm), and the intensity of the E_g and A_{1g} modes accurately for the Fe-doped samples, the broad peak near 600 cm^{-1} was subtracted out. The resulting plots of the Raman peak position, fwhm, and intensity ratios (height and area) vs x are shown in Figure 5a–c, respectively, with the schematic views of the E_g and A_{1g} Raman modes shown in Figure 5d. Figure 5a shows a consistent red-shift for the peaks associated with the E_g and A_{1g} modes vs x; Figure 5b shows a consistent broadening of these peaks; and Figure 5c shows a clear reduction in the relative strength of E_g to A_{1g}. Our discussion of these results is presented below.

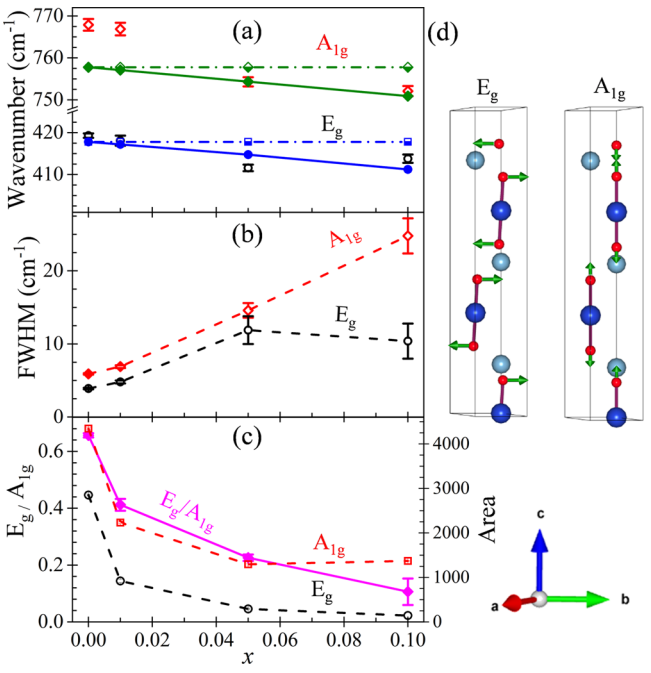

Figure 5. (a) Raman peak positions for the E_g and A_{1g} modes vs x for $CuAl_{1-x}Fe_xO_2$. Experiment, open symbols with error bars; computed using the WDM model, solid symbols connected with solid lines. Half-filled symbols connected with dot-dashed lines show the computed mode frequencies considering only weighted average masses. (b) Experimental fwhm of peaks for E_g and A_{1g} modes vs x, as labeled. (c) Area under the peaks for E_g and A_{1g} modes and area ratios E_g/A_{1g} vs x, as labeled. (d) Schematic views of the E_g and A_{1g} Raman modes, as labeled.

3.2.2.1. Red-Shift of the E_g and A_{1g} Peaks. In Figure 5a, along with the peak positions showing the red-shift with increasing x, the solid lines show WDM computational results for E_g and A_{1g} modes vs x and dot-dashed (horizontal) lines show the computational results for mass weighted average only. The Raman-active E_g and A_{1g} modes involve motion of the oxygen atoms only (see Figure 5d), so their frequencies will not change with Fe content for a model using only the mass weighted average (prediction is horizontal). This lack of agreement with experimental results directly shows the necessity of taking into account the change in both the masses and force constants. The values and trends of calculated frequencies for our WDM approach (mass and force-constant weighted average) agree well with the experimental data. This confirms the red-shift of the optical phonon mode associated with smaller interatomic forces and larger mass, when substituting Al with Fe, even though only the O is vibrating in these modes.

This argument is further strengthened by directly comparing the change in properties from the $CuAlO_2$ end point through to the 10% alloy to the change in properties between the $CuAlO_2$ and end points (for which excellent data is available). For example, as shown in Figure 1a, the lattice expands with Fe doping. The relative expansion along the a-axis is nearly 6 times more than that along c-axis. This difference is in line with the lattice constants of $CuAlO_2$ (a = 2.858, c = 16.958 Å) with the larger unit cell of $CuFeO_2$ (a = 3.035, c = 17.166 Å), which shows an increase of 6.1% along a but only 1.2% along c. Thus, the rate of expansion (shown in Figure 1 for $CuAl_{1-x}Fe_xO_2$) continues until x = 1 ($CuFeO_2$). Consider this analysis for vibrational modes. Specifically, for $CuFeO_2$, the positions of the Raman modes are E_g = 352 cm^{-1} and A_{1g} = 692 cm^{-1},[53] representing a red-shift of the E_g and A_{1g} modes by 70 cm^{-1} (17%) and 80 cm^{-1} (10%), respectively, from the values for $CuAlO_2$. The red-shift of the E_g and A_{1g} modes for x up to 0.10 are 6 cm^{-1} (1.4%) and 17 cm^{-1} (2.2%), respectively. This indicates the observed red-shifts are the result from the expansion of the lattice constant with lengthening of the M–O bonds, which reduces their stiffness and lowers these Raman frequencies. Because Cu, Al, and Fe atoms are stationary in the E_g and A_{1g} modes, their masses should not affect the mode frequencies. Additional support for these arguments comes from a study of the effect of particle size on the Raman spectra and lattice parameters of $CuAlO_2$ nanoparticles down to a size of 10 nm.[48] Here for a particle size of 10 nm, the lattice expands with a = 2.870 Å and c = 16.966 Å compared to a = 2.856 Å and c = 16.931 Å for bulk $CuAlO_2$ (0.35% and 0.21% expansion of a and c, respectively). The Raman modes are red-shifted by ~3% with this increase in unit cell size, with E_g shifting from 419 to 407 cm^{-1} and A_{1g} from 767 to 740 cm^{-1} for the bulk vs 10 nm particles, respectively.

3.2.2.2. Broadening and Relative Intensities of the E_g and A_{1g} Peaks. Figure 5b shows the large broadening of both the E_g and A_{1g} Raman modes with increasing x, and plot (c) shows the sharp decrease in the intensity ratio of the E_g/A_{1g} modes. This is also evident in Figure 3, which shows that the intensity of the E_g mode is reduced with an increase in x, to the point that it is barely noticeable for x = 0.10. The broadening of the modes with Fe doping can be related to the red-shifts, by the following argument. Doping $CuAlO_2$ with Fe produces inhomogeneity in the lattice in that, at sites where Fe replaces Al, the lattice locally behaves as $CuFeO_2$ with its Raman modes red-shifted, whereas at sites without Fe doping the Raman modes locally behave as $CuAlO_2$. Therefore, the addition of a small amount of Fe will lead to heterogeneous broadening toward the low wavenumber side, as observed in Figure 4. Figure 5c shows the behavior of the peak areas of the E_g and A_{1g} modes and their ratio E_g/A_{1g} with increasing x. Both E_g and A_{1g} peaks strongly reduce with increasing x, with E_g decreasing faster than A_{1g}, as indicated by the decrease in the ratio E_g/A_{1g}. These reductions are probably related to the large changes in the electronic band structure of the alloys near the excitation energy of 2.5 eV (488 nm) even for very small x and the effect of disorder associated with doping with Fe. As discussed below, for FTIR spectroscopy, the size of the observed absorption peaks does not change appreciably with x.

3.2.3. FTIR Spectroscopy. Not all the vibrational modes of a system are Raman-active. For this reason, we used FTIR spectroscopy to determine the frequencies of other

DOI: 10.1021/acs.jpcc.9b09402
J. Phys. Chem. C 2019, 123, 30604–30612

$CuAl_{1-x}Fe_xO_2$ vibrational modes to compare with our calculations. The observed FTIR absorbance spectra of the $CuAl_{1-x}Fe_xO_2$ samples (x = 0, 0.01, 0.05, and 0.10) in the 400−1800 cm^{-1} frequency range are shown in Figure 6. (For the 1800−4000 cm^{-1} range, the spectra have no distinct features.) The observed peaks are labeled as A through H in the top panel of Figure 6 for ease of discussion, and in the bottom panel the sources of these peaks are identified.

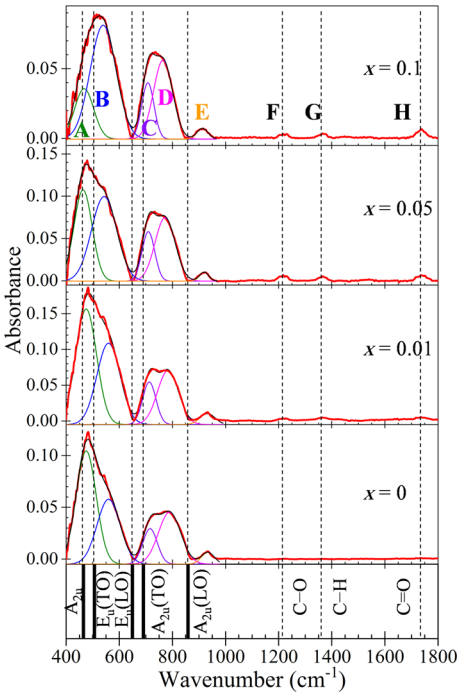

Figure 6. IR absorbance vs wavenumber for $CuAl_{1-x}Fe_xO_2$ (x = 0, 0.01, 0.05, and 0.10). Peaks A−E are labeled by corresponding WDM calculated modes. IR modes are deconvoluted using Gaussian functions (see Table 1). Peaks F−H are from organic contaminants typical for powders in air.

It is noted that the peaks F−H are not associated with vibrational modes of $CuAl_{1-x}Fe_xO_2$ because these peaks are independent of Fe doping and these peaks closely match the frequencies associated with the stretching modes of C−O, C−H, and C═O, respectively. The source of the F−H peaks is adventitious carbon layers that build up on powder samples exposed to air.[54] This agrees with our recently reported XPS studies for these powder samples,[8] where the observed C 1s peaks were identified as adventitious carbon and fitted to alkane (C−H), alcohol (C−OH), and acid-ester (O−C═O) peaks.[55−57]

The peaks labeled A−D in Figure 6 are deconvolved using Gaussian functions, and peaks A−E are identified according to the calculated modes shown in Figure 2a. The positions of all these peaks along with the identified mode computed using our WDM model are listed in Table 1. For modes A−E, the computational values are consistently smaller than our observed values and these modes get red-shifted with an increase in x (except for the A mode for x = 0.10) (see Table 1). To facilitate the comparison between experimental and computational results, the change in the IR-active phonon modes vs x is plotted in Figure 7. The experimental data are shown by open circles with error bars, and the computed trends are indicated by solid squares and lines for the WDM model and half-solid squares and dot-dashed lines for the A_{2u}(LO) mode. The results from the WDM model agree with the experimental results within the associated error bars. The underestimation of vibrational mode wavenumbers may be related to the fact that the calculations are done for 0 K, whereas the experimental measurements are done at room temperature. The schematic vibrational modes are shown in the primitive unit cell for each mode. All atoms are vibrating in the IR-active modes, whereas for the Raman-active modes only oxygen atoms are vibrating. From the phonon dispersion plotted in Figure 2 and considering the propagation wavevector direction, the modes are labeled as LO and TO. The associated propagation wavevector is shown on the schematic vibration mode representations. The A_{2u}(LO) and A_{2u}(TO) modes, both with calculated wavenumber 465 cm^{-1}, are not resolved. Using weighted average masses only (and not the force constants) results in a change in vibration modes with x, as shown by the half-solid symbols connected with the dash-dotted line for the E_u(TO) mode (second panel of Figure 7).

Table 1. DFT-Calculated and Measured Wavenumbers for Identified IR and Raman (R) Modes of $CuAl_{1-x}Fe_xO_2$ for x = 0, 0.01, 0.05, and 0.10 (Same Labels as in Figure 6)[a]

			x							
			0		0.01		0.05		0.10	
modes	Figure 7	activity	DFT	expt	DFT	expt	DFT	expt	DFT	expt
E_u(TO)		IR	153		153		152		150	
E_u(LO)		IR	157		156		155		153	
E_g		R	418	419	417	418	415	410	412	413
A_{2u}(LO)	A	IR	465	475	464	475	458	464	451	468
A_{2u}(TO)										
E_u(TO)	B	IR	507	560	505	560	496	543	486	539
E_u(LO)	C	IR	649	716	647	713	639	709	628	708
A_{2u}(TO)	D	IR	691	789	689	783	683	772	677	765
A_{1g}		R	758	768	757	766	754	754	751	751
A_{2u}(LO)	E	IR	859	934	857	932	850	919	843	913
C−O	F	IR		1216		1217		1217		1217
C−H	G	IR		1364		1365		1365		1363
C═O	H	IR		1735		1735		1735		1736

[a]Peaks F−H are from organic contamination.

DOI: 10.1021/acs.jpcc.9b09402
J. Phys. Chem. C 2019, 123, 30604−30612

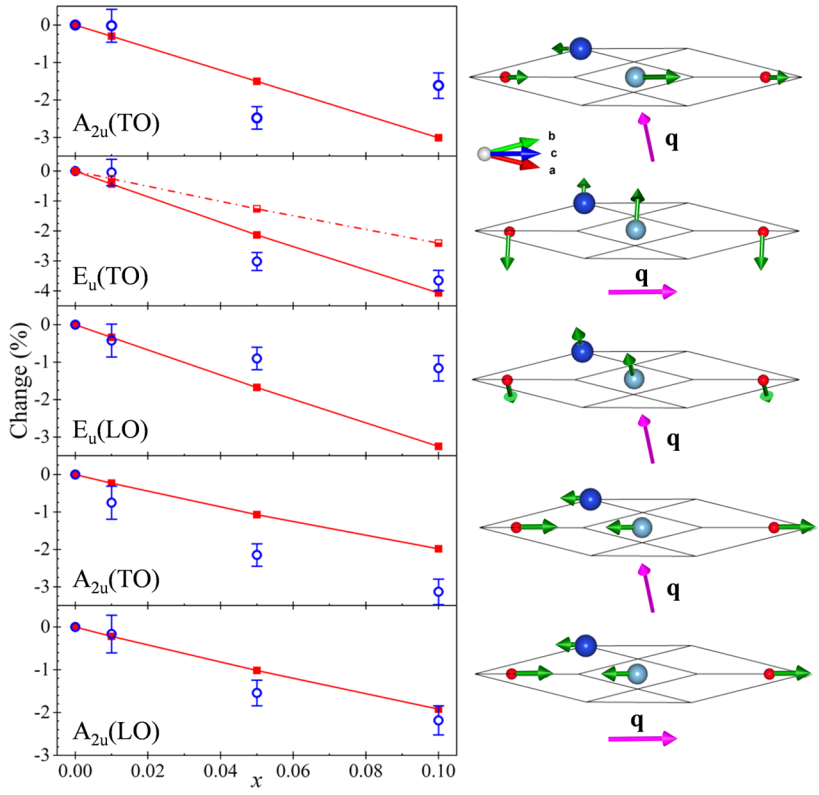

Figure 7. Left: Percentage changes in spectral line position vs x for the IR-active modes. Experiment, circles with error bars; computed, solid squares connected with solid lines. For E_u(TO), half-filled squares connected with a dot-dashed line show the computed mode frequencies considering only weighted average masses. Right: Schematic views of the corresponding IR vibrational modes with propagation wavevector, **q**.

However, the agreement with our experimentally measured modes is not good but it becomes much better when both the masses and force constants are weight-averaged. The case for including the weighted average forces agrees with the findings for the Raman-active modes, discussed above. This directly shows the importance of considering changes in both the force constants and the masses. These red-shifts are qualitatively similar to those observed for the two Raman-active modes discussed earlier and are likely to have a similar origin (see Figure S2, Supporting Information). Regarding the size of the absorption peaks associated with optical phonon modes (peaks A–E), qualitatively, we do not see a strong decrease with x. This is in stark contrast to the large decrease in peak size observed for the Raman peaks. Finally, regarding previous FTIR reports on $CuAl_{1-x}Fe_xO_2$, we are aware of only one brief report by Lv et al.[58] For the x = 0 case, they reported three modes at 513, 711, and 933 cm^{-1}, which agree with the modes B, C, and E in Table 1. For the Fe-doped samples, they reported four modes but their frequencies were not listed or compared to the calculated values in ref 47.

4. SUMMARY AND CONCLUSIONS

In this paper, results have been presented on the phonon modes of $CuAl_{1-x}Fe_xO_2$ computed using several models accompanied by comparison with the experimental data on the Raman and FTIR modes in powder samples of $CuAl_{1-x}Fe_xO_2$. Using a disordered supercell, we model the structure of the lattice and find good agreement with our Rietveld-refined XRD results. For the calculation of lattice dynamics, continuing with this disordered supercell is computationally too demanding. Instead, we introduce an effective medium approach, a weighted dynamical matrix (WDM) approximation method, and compare its results to the frequency modes measured using Raman and FTIR spectroscopy. This WDM approximation weight averages both the force constants and the alloy masses, and we directly show that this results in better agreement with the empirically measured optical phonon spectra than a simpler weight average of the masses only. Raman and FTIR modes for $CuAl_{1-x}Fe_xO_2$ samples with x = 0, 0.01, 0.05, and 0.10 show that the Raman-active modes, E_g (419 cm^{-1}) and A_{1g} (767 cm^{-1}), and the five FTIR modes are red-shifted with an increase in x. The observed frequencies of these Raman and FTIR modes are in good agreement with our calculations using the WDM approximation. These results are also consistent with the lattice expansion accompanying the Fe-doping weakening the M–O bonds (M: Al or Fe).

■ ASSOCIATED CONTENT

Supporting Information

The Supporting Information is available free of charge at https://pubs.acs.org/doi/10.1021/acs.jpcc.9b09402.

XRD spectra, including their Rietveld analysis results and extracted lattice parameters for x = 0.0, 0.01, 0.05, and 0.10; IR-active frequencies plotted vs x for the peaks labeled A–E in Figure 6 (PDF)

■ AUTHOR INFORMATION

Corresponding Author

*E-mail: matthew.johnson@mail.wvu.edu. Phone: 304-293-5136.

DOI: 10.1021/acs.jpcc.9b09402
J. Phys. Chem. C 2019, 123, 30604–30612

ORCID

M. Aziziha: 0000-0003-4001-6413

J. P. Lewis: 0000-0002-6724-3483

A. H. Romero: 0000-0001-5968-0571

Notes

The authors declare no competing financial interest.

■ ACKNOWLEDGMENTS

The authors are thankful for the funding from start-up funds from WVU (MA, MBJ), DOE SC-0004737, DOE SC-0019491, DMREF-NSF 1434897, and NSF OAC-1740111 projects and funding from the Chinese Academy of Sciences President's International Fellowship Initiative (PIFI) for 2017−2018. This work used the computational resources from XSEDE which is supported by National Science Foundation Grant Number ACI-1053575. The authors also acknowledge the support from the Texas Advanced Computing Center (with the Stampede2 and Bridges supercomputers). We thank the Shared Research Facility of West Virginia University for providing and maintaining the XRD instrument used in this project, especially Dr. Qiang Wang.

■ REFERENCES

(1) Kawazoe, H.; Yasukawa, M.; Hyodo, H.; Kurita, M.; Yanagi, H.; Hosono, H. P-Type Electrical Conduction in Transparent Thin Films of $CuAlO_2$. *Nature* **1997**, *389* (6654), 939−942.

(2) Yanagi, H.; Inoue, S.; Ueda, K.; Kawazoe, H.; Hosono, H.; Hamada, N. Electronic Structure and Optoelectronic Properties of Transparent P-Type Conducting $CuAlO_2$. *J. Appl. Phys.* **2000**, *88*, 4159.

(3) Marquardt, M. A.; Ashmore, N. A.; Cann, D. P. Crystal Chemistry and Electrical Properties of the Delafossite Structure. *Thin Solid Films* **2006**, *496* (1), 146−156.

(4) Banerjee, A. N.; Chattopadhyay, K. K. Recent Developments in the Emerging Field of Crystalline P-Type Transparent Conducting Oxide Thin Films. *Prog. Cryst. Growth Charact. Mater.* **2005**, *50* (1−3), 52−105.

(5) Lekse, J. W.; Underwood, M. K.; Lewis, J. P.; Matranga, C. Synthesis, Characterization, Electronic Structure, and Photocatalytic Behavior of $CuGaO_2$ and $CuGa_{1-x}Fe_xO_2$ (x = 0.05, 0.10, 0.15, 0.20) Delafossites. *J. Phys. Chem. C* **2012**, *116* (2), 1865−1872.

(6) Zhao, T.; Liu, Q.-L.; Zhao, Z.-Y. High-Throughput Screening Delafossite $CuMO_2$ (M = IIIA, 3d, 4d, 5d, and RE) Optoelectronic Functional Materials Based on First-Principles Calculations. *J. Phys. Chem. C* **2019**, *123* (23), 14292−14302.

(7) Zamani Meymian, M. R.; Haji Abdolvahab, R.; Kosari Mehr, A. Fractal Characteristics of TiO2-Ag Nanocomposite Films Deposited by a Grid-Assisted Co-Sputtering Method. *Appl. Surf. Sci.* **2019**, *480*, 593−600.

(8) Lee, J.; Petruska, M. A.; Sun, S. Surface Modification and Assembly of Transparent Indium Tin Oxide Nanocrystals for Enhanced Conductivity. *J. Phys. Chem. C* **2014**, *118* (22), 12017−12021.

(9) Pan, Y. Vacancy-Enhanced Cycle Life and Electrochemical Performance of Lithium-Rich Layered Oxide Li2RuO3. *Ceram. Int.* **2019**, *45* (15), 18315−18319.

(10) Pellicer-Porres, J.; Segura, A.; Gilliland, A. S.; Muñoz, A.; Rodríguez-Hernández, P.; Kim, D.; Lee, M. S.; Kim, T. Y. On the Band Gap of CuAlO2 Delafossite. *Appl. Phys. Lett.* **2006**, *88* (18), 181904.

(11) Senty, T. R.; Haycock, B.; Lekse, J.; Matranga, C.; Wang, H.; Panapitiya, G.; Bristow, A. D.; Lewis, J. P. Optical Absorption and Disorder in Delafossites. *Appl. Phys. Lett.* **2017**, *111* (1), 012102.

(12) Körmann, F.; Ikeda, Y.; Grabowski, B.; Sluiter, M. H. F. Phonon Broadening in High Entropy Alloys. *Npj Comput. Mater.* **2017**, *3* (1), 36.

(13) Aziziha, M.; Beesley, R.; Magers, J. R.; Mottaghi, N.; Holcomb, M. B.; Lewis, J. P.; Seehra, M. S.; Johnson, M. B. Electronic State and Concentration of Fe3+ in CuAl1−xFexO2 Determined by Magnetic Measurements. *J. Magn. Magn. Mater.* **2019**, *471*, 495−500.

(14) Aziziha, M.; Byard, S. A.; Beesely, R.; Lewis, J. P.; Seehra, M. S.; Johnson, M. B. Magnetic Properties of Fe-Doped $CuAlO_2$ and Role of Impurities. *AIP Adv.* **2019**, *9* (3), 035030.

(15) Freysoldt, C.; Grabowski, B.; Hickel, T.; Neugebauer, J.; Kresse, G.; Janotti, A.; Van de Walle, C. G. First-Principles Calculations for Point Defects in Solids. *Rev. Mod. Phys.* **2014**, *86* (1), 253−305.

(16) Pan, Y. Theoretical Discovery of High Capacity Hydrogen Storage Metal Tetrahydrides. *Int. J. Hydrogen Energy* **2019**, *44* (33), 18153−18158.

(17) Guc, M.; Tsin, F.; Rousset, J.; Romanyuk, Y. E.; Izquierdo-Roca, V.; Pérez-Rodríguez, A. Nondestructive Raman Scattering Assessment of Solution-Processed ZnO-Doped Layers for Photovoltaic Applications. *J. Phys. Chem. C* **2017**, *121* (6), 3212−3218.

(18) Bellaiche, L.; Vanderbilt, D. Virtual Crystal Approximation Revisited: Application to Dielectric and Piezoelectric Properties of Perovskites. *Phys. Rev. B: Condens. Matter Mater. Phys.* **2000**, *61* (12), 7877−7882.

(19) Gao, M. C. *High-Entropy Alloys*; Springer Science+Business Media: New York, 2016.

(20) Soven, P. Coherent-Potential Model of Substitutional Disordered Alloys. *Phys. Rev.* **1967**, *156* (3), 809−813.

(21) Tian, F. A Review of Solid-Solution Models of High-Entropy Alloys Based on Ab Initio Calculations. *Front. Mater.* **2017**, *4*, 36.

(22) Feynman, R. P. Forces in Molecules. *Phys. Rev.* **1939**, *56* (4), 340−343.

(23) Klemens, P. G. The Scattering of Low-Frequency Lattice Waves by Static Imperfections. *Proc. Phys. Soc., London, Sect. A* **1955**, *68* (12), 1113−1128.

(24) Seyf, H. R.; Henry, A. A Method for Distinguishing between Propagons, Diffusions, and Locons. *J. Appl. Phys.* **2016**, *120* (2), 025101.

(25) Seyf, H. R.; Yates, L.; Bougher, T. L.; Graham, S.; Cola, B. A.; Detchprohm, T.; Ji, M.-H.; Kim, J.; Dupuis, R.; Lv, W. Rethinking Phonons: The Issue of Disorder. *Npj Comput. Mater.* **2017**, *3* (1), 49.

(26) Ghosh, S.; Leath, P. L.; Cohen, M. H. Phonons in Random Alloys: The Itinerant Coherent-Potential Approximation. *Phys. Rev. B: Condens. Matter Mater. Phys.* **2002**, *66* (21), 214206.

(27) Wang, Y.; Zacherl, C. L.; Shang, S.; Chen, L.-Q.; Liu, Z.-K. Phonon Dispersions in Random Alloys: A Method Based on Special Quasi-Random Structure Force Constants. *J. Phys.: Condens. Matter* **2011**, *23* (48), 485403.

(28) de Gironcoli, S. Phonons in Si-Ge Systems: An *Ab Initio* Interatomic-Force-Constant Approach. *Phys. Rev. B: Condens. Matter Mater. Phys.* **1992**, *46* (4), 2412−2419.

(29) Cheng, Z.; Zhai, J.; Zhang, Q.; Ke, Y. Auxiliary Coherent Medium Theory for Lattice Vibrations in Random Binary Alloys with Mass and Force-Constant Disorders. *Phys. Rev. B: Condens. Matter Mater. Phys.* **2019**, *99* (13), 134202.

(30) Koniakhin, S. V.; Utesov, O. I.; Terterov, I. N.; Siklitskaya, A. V.; Yashenkin, A. G.; Solnyshkov, D. Raman Spectra of Crystalline Nanoparticles: Replacement for the Phonon Confinement Model. *J. Phys. Chem. C* **2018**, *122* (33), 19219−19229.

(31) Amrute, A. P.; Łodziana, Z.; Mondelli, C.; Krumeich, F.; Pérez-Ramírez, J. Solid-State Chemistry of Cuprous Delafossites: Synthesis and Stability Aspects. *Chem. Mater.* **2013**, *25* (21), 4423−4435.

(32) Kresse, G.; Furthmüller, J. Efficiency of Ab-Initio Total Energy Calculations for Metals and Semiconductors Using a Plane-Wave Basis Set. *Comput. Mater. Sci.* **1996**, *6* (1), 15−50.

(33) Kresse, G.; Furthmüller, J.; Hafner, J. *Ab Initio* Force Constant Approach to Phonon Dispersion Relations of Diamond and Graphite. *Europhys. Lett. (EPL)* **1995**, *32* (9), 729−734.

(34) Kresse, G.; Joubert, D. From Ultrasoft Pseudopotentials to the Projector Augmented-Wave Method. *Phys. Rev. B: Condens. Matter Mater. Phys.* **1999**, *59* (3), 1758−1775.

DOI: 10.1021/acs.jpcc.9b09402
J. Phys. Chem. C 2019, 123, 30604−30612

(35) Blöchl, P. E. Projector Augmented-Wave Method. *Phys. Rev. B: Condens. Matter Mater. Phys.* **1994**, *50* (24), 17953−17979.
(36) Grau-Crespo, R.; Hamad, S.; Catlow, C. R. A.; Leeuw, N. H. de. Symmetry-Adapted Configurational Modelling of Fractional Site Occupancy in Solids. *J. Phys.: Condens. Matter* **2007**, *19* (25), 256201.
(37) Csonka, G. I.; Perdew, J. P.; Ruzsinszky, A.; Philipsen, P. H. T.; Lebègue, S.; Paier, J.; Vydrov, O. A.; Ángyán, J. G. Assessing the Performance of Recent Density Functionals for Bulk Solids. *Phys. Rev. B: Condens. Matter Mater. Phys.* **2009**, *79* (15), 155107.
(38) Aziziha, M.; Motamedifar, M.; Mahdavifar, S. Multicritical Point in the One-Dimensional Quantum Compass Model. *Acta Phys. Pol., B* **2013**, *44* (2), 221.
(39) Barker, A. S.; Merz, J. L.; Gossard, A. C. Study of Zone-Folding Effects on Phonons in Alternating Monolayers of GaAs-AlAs. *Phys. Rev. B: Condens. Matter Mater. Phys.* **1978**, *17* (8), 3181−3196.
(40) Romero, A. H.; Cardona, M.; Kremer, R. K.; Lauck, R.; Siegle, G.; Serrano, J.; Gonze, X. C. Lattice Properties of Pb X (X = S, Se, Te) : Experimental Studies and *Ab Initio* Calculations Including Spin-Orbit Effects. *Phys. Rev. B: Condens. Matter Mater. Phys.* **2008**, *78* (22), 224302.
(41) Etchegoin, P. G.; Cardona, M.; Lauck, R.; Clark, R. J. H.; Serrano, J.; Romero, A. H. Temperature-Dependent Raman Scattering of Natural and Isotopically Substituted PbS. *Phys. Status Solidi B* **2008**, *245* (6), 1125−1132.
(42) Togo, A.; Tanaka, I. First Principles Phonon Calculations in Materials Science. *Scr. Mater.* **2015**, *108*, 1−5.
(43) Bish, D. L.; Howard, S. A. Quantitative Phase Analysis Using the Rietveld Method. *J. Appl. Crystallogr.* **1988**, *21*, 86−91.
(44) De La Torre, A. G.; Bruque, S.; Aranda, M. A. G. Rietveld Quantitative Amorphous Content Analysis. *J. Appl. Crystallogr.* **2001**, *34* (2), 196−202.
(45) Vegard, L. VI. Results of Crystal Analysis. *London, Edinburgh, and Dublin Philosophical Magazine and Journal of Science* **1916**, *32* (187), 65−96.
(46) Vegard, L. LV. Results of Crystal Analysis.—III. *London, Edinburgh, and Dublin Philosophical Magazine and Journal of Science* **1916**, *32* (191), 505−518.
(47) Pellicer-Porres, J.; Martínez-García, D.; Segura, A.; Rodríguez-Hernández, P.; Muñoz, A.; Chervin, J. C.; Garro, N.; Kim, D. Pressure and Temperature Dependence of the Lattice Dynamics of CuAlO2 Investigated by Raman Scattering Experiments and *Ab Initio* Calculations. *Phys. Rev. B: Condens. Matter Mater. Phys.* **2006**, *74* (18), 184301.
(48) Yassin, O. A.; Alamri, S. N.; Joraid, A. A. Effect of Particle Size and Laser Power on the Raman Spectra of $CuAlO_2$ Delafossite Nanoparticles. *J. Phys. D: Appl. Phys.* **2013**, *46* (23), 235301.
(49) Liu, R.; Li, Y.; Yao, B.; Ding, Z.; Deng, R.; Zhang, L.; Zhao, H.; Liu, L. Experimental and First-Principles Study of Photoluminescent and Optical Properties of Na-Doped $CuAlO_2$: The Role of the $Na_{Al}-2Na_i$ Complex. *J. Phys. D: Appl. Phys.* **2015**, *48* (33), 335102.
(50) Lan, W.; Pan, J. Q.; Zhu, C. Q.; Wang, G. Q.; Su, Q.; Liu, X. Q.; Xie, E. Q.; Yan, H. Role of Oxygen in Structural Properties of Annealed CuAlO2 Films. *J. Cryst. Growth* **2011**, *314* (1), 370−373.
(51) Garg, A.; Rao, R. Copper Delafossites under High Pressure—A Brief Review of XRD and Raman Spectroscopic Studies. *Crystals* **2018**, *8* (6), 255.
(52) Seehra, M. S.; Narang, V.; Geddam, U. K.; Stefaniak, A. B. Correlation between X-Ray Diffraction and Raman Spectra of 16 Commercial Graphene−Based Materials and Their Resulting Classification. *Carbon* **2017**, *111*, 380−385.
(53) Salke, N. P.; Kamali, K.; Ravindran, T. R.; Balakrishnan, G.; Rao, R. Raman Spectroscopic Studies of CuFeO2 at High Pressures. *Vib. Spectrosc.* **2015**, *81*, 112−118.
(54) Barr, T. L.; Seal, S. Nature of the Use of Adventitious Carbon as a Binding Energy Standard. *J. Vac. Sci. Technol., A* **1995**, *13* (3), 1239.
(55) Barbara, H. S. *Infrared Spectroscopy: Fundamentals and Applications*; Analytical Techniques in the Sciences; John Wiley & Sons, Ltd, 2004.
(56) Smith, B. C. *Infrared Spectral Interpretation: A Systematic Approach*, 1st ed.; CRC Press: Boca Raton, FL, 2018.
(57) Coates, J. Interpretation of Infrared Spectra, A Practical Approach. In *Encyclopedia of Analytical Chemistry*; John Wiley & Sons, Ltd.: 2006; DOI: 10.1002/9780470027318.a5606.
(58) Lv, C.; Huang, Y.; Feng, M.; Long, M.; Zhang, C. Structure and Infrared Optical Properties Research on Fe-Doped $CuAlO_2$ Semiconductor. In *Proceedings of the 5th International Conference on Advanced Design and Manufacturing Engineering*; Atlantis Press: Shenzen, China, 2015; DOI: 10.2991/icadme-15.2015.350.

DOI: 10.1021/acs.jpcc.9b09402
J. Phys. Chem. C 2019, 123, 30604−30612